

# **Study the quantum resolution sizes and atomic bonding states of two-dimensional tin monoxide**

Yu Wang, Yunhu Zhu, Yixin Li, Maolin Bo\*

Key Laboratory of Extraordinary Bond Engineering and Advanced Materials Technology (EBEAM) of Chongqing, Yangtze Normal University, Chongqing 408100, China

\*Author to whom correspondence should be addressed: bmlwd@yznu.edu.cn (Maolin Bo)

## **Abstract**

Understanding the interatomic bonding and electronic properties of two-dimensional (2D) materials is crucial for preparing high-performance 2D semiconductor materials. We have calculated the band structure, electronic properties, and bonding characteristics of SnO in 2D materials by using density functional theory (DFT) and combining bond energy and bond charge models. Atomic bonding analysis enables us to deeply and meticulously analyze the interatomic bonding and charge transfer in the layered structure of SnO. This study greatly enhances our understanding of the local bonding state on the surface of 2D structural materials. In addition, we use the renormalization method to operate energy to determine the wave function at different quantum resolutions. This is of great significance for describing the size and phase transition of nanomaterials.

**Keywords:** 2D material SnO, DFT Calculations, Electronic Structure

## 1. Introduction

Two-dimensional(2D) materials, owing to their unique physical and chemical properties, have demonstrated tremendous application potential in numerous fields such as electronics, optics, and energy[1-3]. In recent years, research on SnO in 2D materials has garnered significant attention. The interlayer bonding mode of this type of material differs from that of traditional van der Waals materials[3, 4]. It is typically connected by metal bonds or electrostatic interactions, and there is strong electronic coupling. The band gap of SnO can be adjusted over a wide range, ranging from 0.60 eV in the infrared range of bulk samples to 3.65 eV in the ultraviolet range of monolayer samples[5].

In the field of electrode materials, SnO has significant advantages. Its high electron mobility gives it great potential in electrode materials[6, 7]. The semi-metallicity of SnO is extremely valuable in spintronics[8, 9]. Complete spin-polarized semi-metallicity can be achieved through hole doping and it can be used to design and manufacture efficient spin filters and other devices. Moreover, its strong tunability of band gap can further optimize the semi-metallicity to meet different needs. At present, SnO has great application potential in the fields of electrode materials and spintronics. At the same time, it is also worthy of in-depth exploration in many fields such as photocatalysis, sensors, quantum computing and biomedicine[10-15].

This study employs the DFT calculation method to conduct in-depth research on the band structure, density of states, and properties related to energy renormalization of two-dimensional SnO materials. It calculates the electronic properties and bonding states of 2D SnO materials, revealing the bonding characteristics of these materials at the electronic and atomic levels. This research not only provides a theoretical foundation for understanding the intrinsic properties of 2D SnO compounds but also indicates the direction for the design and optimization of related 2D materials. The exploration of these characteristics is conducive to promoting the development of the field of 2D materials and providing strong support for the development of new materials and technologies.

## 2.Methods

### 2.1 DFT Calculation

The atomic bonding, electronic properties, and structural relaxation of bilayer SnO materials were investigated using the Cambridge Sequential Total Energy Package (CASTEP), which employs total energy with a plane-wave pseudopotential. This analysis centered on the bonding, structure, energetics, and electronic properties of bilayer SnO materials. We utilized the HSE06 hybrid density function to describe their electron exchange and correlation potentials[16]. Additionally, we employed the TS scheme for DFT-D dispersion correction to take into account the long-range van der Waals interaction. All the structures were fully optimized without any symmetry constraints until the force was less than 0.01 eV/Å and the energy tolerances were less than  $5.0 \times 10^{-6}$  eV per atom. A convergence threshold of  $1.0 \times 10^{-6}$  eV/atom was selected for the self-consistent field (SCF) calculations. A vacuum space of at least 14 Å in the direction normal to the bilayer was used to avoid the interaction between periodic images. The cutoff energy, band gaps, and k-point grids are as shown in **Table 1**.

**Table 1** Cut-off energies, band gaps, and  $k$ -points of SnO

Element	Cut-off energy	$k$ -point	Band gap(HSE06)
SnO( $\alpha$ )	750 eV	10×10×2	1.508eV
SnO( $\beta$ )	750 eV	10×10×2	1.090 eV

### 2.2 Renormalization group method

Based on the Kardar-Parisi-Zhang (KPZ) equation[17], the functional integral, that is, the path integral, is calculated:

$$Z(\Lambda) = \int_{\Lambda} \mathcal{D}h e^{-S(h)} \quad (1)$$

Where the action is:

$$S(h) = \frac{1}{2} \int d^D x dt \left[ \frac{\partial h}{\partial t} - \nabla^2 h - \frac{g}{2} (\nabla h)^2 \right]^2 \quad (2)$$

**Eq. 2** defines a field theory. Just like all other field theories, a cutoff parameter  $\Lambda$  needs to be introduced. Now, we integrate a part of field configurations  $h(\mathbf{x}, t)$  separately. All Fourier components  $\mathbf{k}$  and  $\omega$  of this part of field configurations satisfy being no greater than a certain value  $\Lambda$ . In principle, since this is a non-relativistic theory,  $\mathbf{k}$  and  $\omega$  must be cutoff respectively. Here, for the sake of simplified expression, they are collectively referred to as  $\Lambda$ .

From a physical perspective, since the random driving term is white noise  $\eta(\mathbf{x}, t)$ , meaning that at positions  $\mathbf{x}$  and  $\mathbf{x}'$  (similar for different times), they are uncorrelated. Therefore, at the microscopic scale, the surface should be extremely uneven, as shown in **Fig.1(a)**. This study only focuses on physical phenomena at scale  $L$ . Therefore, we intend to put on a “blurred pair of glasses”. At this time, the surface will look like that in **Fig.1(b)**.

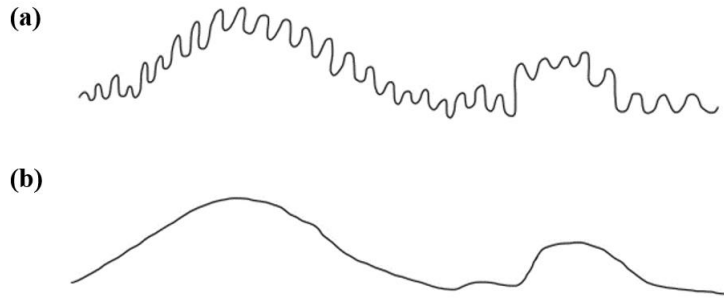


**Fig. 1** White noise of different sizes (a) Small scale (b) Large scale

The renormalization group is just such a set of formal methods linking different scales, namely different energy standards. To realize this physical idea, the length scale can be changed in the functional integral **Eq. 1**. In Euclidean space  $\lambda\varphi^4$  theory[18]:

$$Z(\Lambda) = \int_{\Lambda} \mathcal{D}\varphi e^{-\int d^d x \mathcal{L}(\varphi)} \quad (3)$$

Among them, the symbol  $\int_{\Lambda}$  indicates an integration that is limited to field configurations where  $\varphi(x)$  is defined by the integral  $\varphi(x) = \int \left[ d^d k / (2\pi)^d \right] e^{ikx} \varphi(k)$ .

The function  $\varphi(k)$  is zero for any  $k$  whose magnitude, given by  $|k| \equiv \left( \sum_{i=1}^d k_i^2 \right)^{\frac{1}{2}}$ , exceeds the cutoff  $\Lambda$ . The resolution of the system is inversely related to  $\Lambda$ , with  $L=1 / \Lambda$ .

Let  $\Lambda \rightarrow \Lambda - \delta\Lambda$  (with  $\delta\Lambda > 0$ ) to introduce a degree of blur. The field  $\varphi$  is decomposed into  $\varphi = \varphi_s + \varphi_w$ , where  $s$  represents the smooth component and  $w$  represents the wiggly component. The Fourier components  $\varphi_s(k)$  and  $\varphi_w(k)$  are non-zero only within specific ranges of  $k$ :  $\varphi_s(k)$  is non-zero for  $|k| \leq q(\Lambda - \delta\Lambda)$  and  $\varphi_w(k)$  is non-zero for  $(\Lambda - \delta\Lambda) \leq q|k| \leq q\Lambda$ . By substituting these into **Eq. 3**, the following result can be derived:

$$Z(\Lambda) = \int_{\Lambda - \delta\Lambda} \mathcal{D}\varphi_s e^{-\int d^d x \mathcal{L}(\varphi_s)} \int \mathcal{D}\varphi_w e^{-\int d^d x \mathcal{L}_1(\varphi_s, \varphi_w)} \quad (4)$$

In the expression  $\mathcal{L}_1(\varphi_s, \varphi_w)$ , all terms depend on  $\varphi_w$ . Integrating over  $\varphi_w$ , the result is

$$e^{-\int d^d x \delta \mathcal{L}(\varphi_s)} \equiv \int \mathcal{D}\varphi_w e^{-\int d^d x \mathcal{L}_1(\varphi_s, \varphi_w)} \quad (5)$$

Thus, it follows that

$$Z(\Lambda) = \int_{\Lambda - \delta\Lambda} \mathcal{D}\varphi_s e^{-\int d^d x [\mathcal{L}_1(\varphi_s) + \delta \mathcal{L}(\varphi_s)]} \quad (6)$$

At this point, formally speaking, the theory is now entirely described by the "smooth" field  $\varphi_s$ .

Consider the general expression  $\mathcal{L} = \frac{1}{2}(\partial\varphi)^2 + \sum_n \lambda_n \varphi^n + \dots$ , where  $\lambda_2$  corresponds to  $\frac{1}{2}m^2$  and  $\lambda_4$  is denoted by  $\lambda$ . The terms involving  $\partial\varphi_s$ ,  $\partial\varphi_w$ , among others, integrate to zero, leading to:

$$\int d^d x \mathcal{L}_1(\varphi_s, \varphi_w) = \int d^d x \left( \frac{1}{2}(\partial\varphi_w)^2 + \frac{1}{2}m^2\varphi_w^2 + \dots \right) \quad (7)$$

In the given context,  $\varphi_s$  is included within  $(\dots)$ . This theory describes the interaction of the  $\varphi_w$  field with itself and the background field  $\varphi_s(x)$ .

From the perspective of symmetry, it is known that  $\partial\mathcal{L}(\varphi_s)$  has the same form as  $\mathcal{L}(\varphi_s)$ , differing only in the coefficients. By adding  $\partial\mathcal{L}(\varphi_s)$  to  $\mathcal{L}(\varphi_s)$ , the coupling constants  $\lambda_n$  (as well as the coefficient of  $\frac{1}{2}(\partial\varphi_s)^2$ ) are altered. These changes lead to the flow within the previously described space of coupled functions.

Comparing **Eq. 6** with **Eq. 1**, replace  $\int_{\Lambda-\delta\Lambda}$  in **Eq. 6** with  $\int_{\Lambda}$ , and introduce a real number  $b < 1$  such that  $\Lambda - \delta\Lambda = b\Lambda$ . In  $\int_{\Lambda-\delta\Lambda}$ , the field integration is conducted for fields satisfying  $|k| \leq b\Lambda$ . Perform a simple variable substitution with  $k = -bk'$ , where  $|k'| \leq \Lambda$ . Then, take  $x = x'/b$  to ensure  $e^{ikx} = e^{ik'x'}$ . Substituting these transformations, the following is obtained:

$$\int d^d x \mathcal{L}(\varphi_s) = \int d^d x' b^{-d} \left[ \frac{1}{2} b^2 (\partial' \varphi_s)^2 + \sum_n \lambda_n \varphi_s^n + \dots \right] \quad (8)$$

In the text,  $\partial' = \partial / \partial x' = (1/b) \partial / \partial x$ . The expression  $\varphi'$  is defined as  $b^{2-d} (\partial' \varphi_s)^2 = (\partial' \varphi')^2$ , which implies that  $\varphi' = b^{\frac{1}{2}(2-d)} \varphi_s$ . Consequently, Eq. 8 is transformed into

$$\int d^d x \mathcal{L}(\varphi_s) = \int d^d x' \left[ \frac{1}{2} (\partial' \varphi')^2 + \sum_n \lambda_n b^{-d+(n/2)(d-2)} \varphi'^n + \dots \right] \quad (9)$$

Therefore, the coefficient  $\lambda'_n$  for  $\varphi'^n$  can be written as

$$\lambda'_n = b^{(n/2)(d-2)-d} \lambda_n \quad (10)$$

In which,  $n$  indicates the number of fields interacting with each other, and  $d$  denotes

the dimension.

### 2.3 BBC model

BBC models consist of the binding energy model (BC), bond charge model (BC), and Hamiltonian of the BB model. According to the tight-binding approximation model of band theory[19, 20]:

$$E(\vec{k}) = \varepsilon_i - J_0 - \sum_{R_s} J(\vec{R}_s) e^{-i\vec{k} \cdot \vec{R}_s} \quad (11)$$

$$\text{Among them, } J_0 = - \int \varphi^*_i(\vec{r} - \vec{R}_m) (V(\vec{r}) - v_a(\vec{r} - \vec{R}_m)) \varphi_i(\vec{r} - \vec{R}_m) d\vec{r} ,$$

$$\varepsilon_i = \int \varphi^*_i(\vec{r} - \vec{R}_m) \left( -\frac{\hbar^2}{2m} \nabla^2 + v_a(\vec{r} - \vec{R}_m) \right) \varphi_i(\vec{r} - \vec{R}_m) d\vec{r} ,$$

$$\int \varphi^*_i[\vec{\xi} - (\vec{R}_n - \vec{R}_m)] [V(\vec{\xi}) - v(\vec{\xi})] \varphi_i(\vec{\xi}) d\vec{\xi} = -J(\vec{R}_n - \vec{R}_m) , \quad \vec{\xi} = \vec{r} - \vec{R}_m , \quad \vec{R}_s = \vec{R}_n - \vec{R}_m .$$

For the core electron energy levels, the effect of the exchange integral can be neglected,  $J_0 \gg J(\vec{R}_s)$ . The binding energy shifts of the bulk and surface atoms can be expressed as:

$$E_V(B) - E_V(0) = E_V(k) - \varepsilon_i \approx J_0 . \quad (12)$$

Then , we have  $\Delta E_v(i) = \gamma^m J_0$ .

Further based on  $\psi_k(\vec{r}) = \frac{1}{N} \sum_m e^{i\vec{k} \cdot \vec{R}_m} \varphi_i(\vec{r} - \vec{R}_m)$  ,  $V_{cry}(\vec{r}) = V(\vec{r}) - v_a(\vec{r} - \vec{R}_m)$

and  $\gamma V_{cry}(\vec{r}) = \gamma \sum_{i,j,\vec{R}_j \neq 0} \frac{1}{4\pi\epsilon_0} \frac{Z'e^2}{|\vec{r}_i - \vec{R}_j|}$ . For atomic bonding , the **Eq.12** can be written as:

$$\gamma^m = \frac{E_V(i) - E_V(0)}{E_V(B) - E_V(0)} = \left( \frac{E_V(x) - E_V(0)}{E_V(B) - E_V(0)} \right)^m \approx \left( \frac{Z_x d_b}{Z_b d_x} \right)^m = \left( \frac{Z_b - \mu_v}{Z_b} \right)^m \left( \frac{d_x}{d_b} \right)^{-m} = \left( \frac{d_x}{d_b} \right)^{-m'} \approx \left( \frac{d_x}{d_b} \right)^{-m}$$

$$\ln m' = m \left( 1 - \frac{\ln \frac{Z_b - \mu_v}{Z_b}}{\ln \left( \frac{d_x}{d_b} \right)} \right), \quad \mu_v \text{ is very small; therefore, } \frac{Z_b - \mu_v}{Z_b} \approx 1 \quad \text{and}$$

$m \approx m'$ . For compounds,  $m \neq 1$ .

The Hamiltonian of a system in the BC model is expressed as:

$$H = \sum_{k\sigma} \frac{\hbar^2 k^2}{2m} a_{k\sigma}^\dagger a_{k\sigma} + \frac{e_1^2}{2V} \sum_q \sum_{\bar{k}\sigma} \sum_{\bar{K}'\lambda} \frac{4\pi}{q} a_{\bar{k}+\bar{q},\sigma}^\dagger a_{\bar{K}'-\bar{q},\lambda}^\dagger a_{\bar{K}'\lambda} a_{\bar{k}\sigma} \quad (13)$$

The electron-interaction terms for density fluctuations, which are primarily caused by electrostatic shielding through electron exchange, are given by:

$$\begin{aligned} \delta V_{bc} &= V'_{ee} - V_{ee} \\ &= \frac{e_1^2}{2V} \sum_{\bar{k}} \sum_{\bar{K}'} \sum_{\bar{q}} \sum_{\sigma\lambda} \frac{4\pi}{q^2 + \mu^2} a_{\bar{k}+\bar{q},\sigma}^\dagger a_{\bar{K}'-\bar{q},\lambda}^\dagger a_{\bar{K}'\lambda} a_{\bar{k}\sigma} - \frac{e_1^2}{2V} \sum_q \sum_{\bar{k}\sigma} \sum_{\bar{K}'\lambda} \frac{4\pi}{q^2} a_{\bar{k}+\bar{q},\sigma}^\dagger a_{\bar{K}'-\bar{q},\lambda}^\dagger a_{\bar{K}'\lambda} a_{\bar{k}\sigma} \\ &= \frac{1}{4\pi\epsilon_0} \frac{e^2}{2|\vec{r}-\vec{r}'|} \int d^3r \int d^3r' \rho(\vec{r}) \rho(\vec{r}') e^{-\mu(\vec{r}-\vec{r}')} - \frac{1}{4\pi\epsilon_0} \frac{e^2}{2|\vec{r}-\vec{r}'|} \int d^3r \int d^3r' \rho(\vec{r}) \rho(\vec{r}') \end{aligned} \quad (14)$$

The deformation bond energy  $\delta V_{bc}$  can be represented as:

$$\delta V_{bc} = \frac{1}{4\pi\epsilon_0} \frac{e^2}{2|\vec{r}-\vec{r}'|} \int d^3r \int d^3r' \delta\rho(\vec{r}) \delta\rho(\vec{r}') \quad (15)$$

Also,  $\delta\rho$  satisfies the following relationship

$$\left( \delta\rho_{\text{Hole-electron}} \leq \delta\rho_{\text{Antibonding-electron}} < \delta\rho_{\text{No charge transfer}} = 0 < \delta\rho_{\text{Nonbonding-electron}} \leq \delta\rho_{\text{Bonding-electron}} \right) \quad (16)$$

For atomic (strong) bonding-states:

$$\delta\rho_{\text{Hole-electron}}(\vec{r}) \delta\rho_{\text{Bonding-electron}}(\vec{r}') < 0 \text{ (Strong Bonding)} \quad (17)$$

For atomic nonbonding or weak-bonding states:



$$\left\{ \begin{array}{l} \delta\rho_{Hole-electron}(\vec{r})\delta\rho_{Nonbonding-electron}(\vec{r}') < 0(\text{Nonbonding or Weak Bonding}) \\ \delta\rho_{Antibonding-electron}(\vec{r})\delta\rho_{Bonding-electron}(\vec{r}') < 0(\text{Nonbonding or Weak Bonding}) \\ \delta\rho_{Antibonding-electron}(\vec{r})\delta\rho_{Nonbonding-electron}(\vec{r}') < 0(\text{Nonbonding}) \end{array} \right. \quad (18)$$

For atomic antibonding-states:

$$\left\{ \begin{array}{l} \delta\rho_{Nonbonding-electron}(\vec{r})\delta\rho_{Bonding-electron}(\vec{r}') > 0(\text{Antibonding}) \\ \delta\rho_{Hole-electron}(\vec{r})\delta\rho_{Antibonding-electron}(\vec{r}') > 0(\text{Antibonding}) \\ \delta\rho_{Hole-electron}(\vec{r})\delta\rho_{Hole-electron}(\vec{r}') > 0(\text{Antibonding}) \\ \delta\rho_{Antibonding-electron}(\vec{r})\delta\rho_{Antibonding-electron}(\vec{r}') > 0(\text{Antibonding}) \\ \delta\rho_{Nonbonding-electron}(\vec{r})\delta\rho_{Nonbonding-electron}(\vec{r}') > 0(\text{Antibonding}) \\ \delta\rho_{Bonding-electron}(\vec{r})\delta\rho_{Bonding-electron}(\vec{r}') > 0(\text{Antibonding}) \end{array} \right. \quad (19)$$

The formation of chemical bonds is related to fluctuations in electron density

$\delta\rho$ .

### 3. Results and Discussion

#### 3.1 Geometry structure

The geometric structures of SnO( $\alpha$ ) and SnO( $\beta$ ) are shown in **Fig. 2**. The Sn and O atoms are in an alternating Sn<sub>1/2</sub>-O-Sn<sub>1/2</sub> layered sequence along the [001] crystallographic direction. We optimized the geometric structures of SnO( $\alpha$ ) and SnO( $\beta$ ) using DFT calculations. The optimized lattice parameters, bond lengths, bond angles, and interlayer distance are shown in **Table 2**. In the two different crystal structures of SnO( $\alpha$ ) and SnO( $\beta$ ), the changes in the atomic radii and electronegativities of tin (Sn) atoms and oxygen (O) atoms respectively will lead to slight differences in the interlayer distances. Specifically, the measured interlayer distance of SnO( $\alpha$ ) is 2.792 Å, while that of SnO( $\beta$ ) is 2.744 Å. The Sn - O bond length of SnO( $\alpha$ ) is 2.260 Å, which is slightly longer compared to 2.256 Å of SnO( $\beta$ ). The bond angles of the two crystal forms are 118.01° and 118.09° respectively. Meanwhile, we also used molecular dynamics to simulate and calculate the stability of SnO( $\alpha$ ) and SnO( $\beta$ ). The results of molecular dynamics simulations clearly demonstrate that both of SnO( $\alpha$ ) and SnO( $\beta$ ) possess good stability.

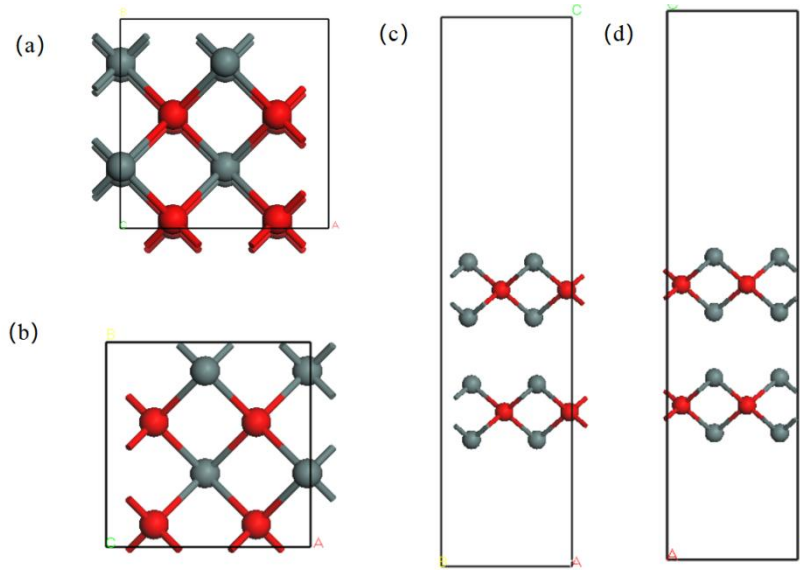


**Fig. 2** (a) and (c) show the crystal structure of SnO( $\alpha$ ), while (b) and (d) present the crystal structure of SnO( $\beta$ ).

**Table 2** Bond length, bond angle, interlayer distance and lattice parameters of 2D SnO( $\alpha$ ) and SnO( $\beta$ )

	Interlayer distance (Å)	Lattice parameters (° / Å)						Bond length (Å)	Bond angle (°)
		$\alpha$	$\beta$	$\gamma$	a	b	c		
SnO( $\alpha$ )	2.792	90	90	90	5.474	5.476	23.000	2.260	118.01 (Sn-O-Sn)
SnO( $\beta$ )	2.744	90	90	90	5.474	5.476	23.000	2.256	118.09 (Sn-O-Sn)

### 3.2 Band structure, density of states, and deformation charge density

Each oxygen (O) atom coordinates with four surface metal tin (Sn) atoms, thus constructing the Sn - O tetrahedral structure. Due to its unique band structure, the valence band maximum (VBM) is mainly composed of the 5s orbital of Sn and the 2p orbital of O. Among them, the lone electron pair formed by the 5s orbital of Sn points to the interlayer spacing, and there is a strong dipole-dipole interaction between adjacent SnO layers. The band structure diagram of SnO along the special wave vector symmetry points in the Brillouin zone calculated by DFT shows that in **Fig. 3**, the Fermi level  $E_f$  is located at the position where the energy is 0. By observing the calculated band structure diagram, it can be found that the conduction band of SnO is in the region above the Fermi surface, and the valence band is located in the region

below the Fermi surface. The highest point of the valence band and the lowest point of the conduction band are both located at the G point in the Brillouin zone. These two points are close to each other and are respectively distributed at both ends of the Fermi surface. Moreover, the valence band is closer to the Fermi level, and even one valence band line coincides with the Fermi level. It can be inferred from this that SnO belongs to a direct narrow bandgap semiconductor material. It can also be further known from the calculation results that the bandgaps of SnO( $\alpha$ ) and SnO( $\beta$ ) are 1.153 eV and 1.090 eV respectively. Meanwhile, it can be seen from the distribution pattern of electrons in the Brillouin zone in the figure that the bandgap between the F and Q regions is the largest, and the band structure in the F to Q region of the Brillouin zone shows a relatively large bandgap and highly coincident energy level lines, which indicates that SnO has excellent electron transport properties and good stability in this direction.

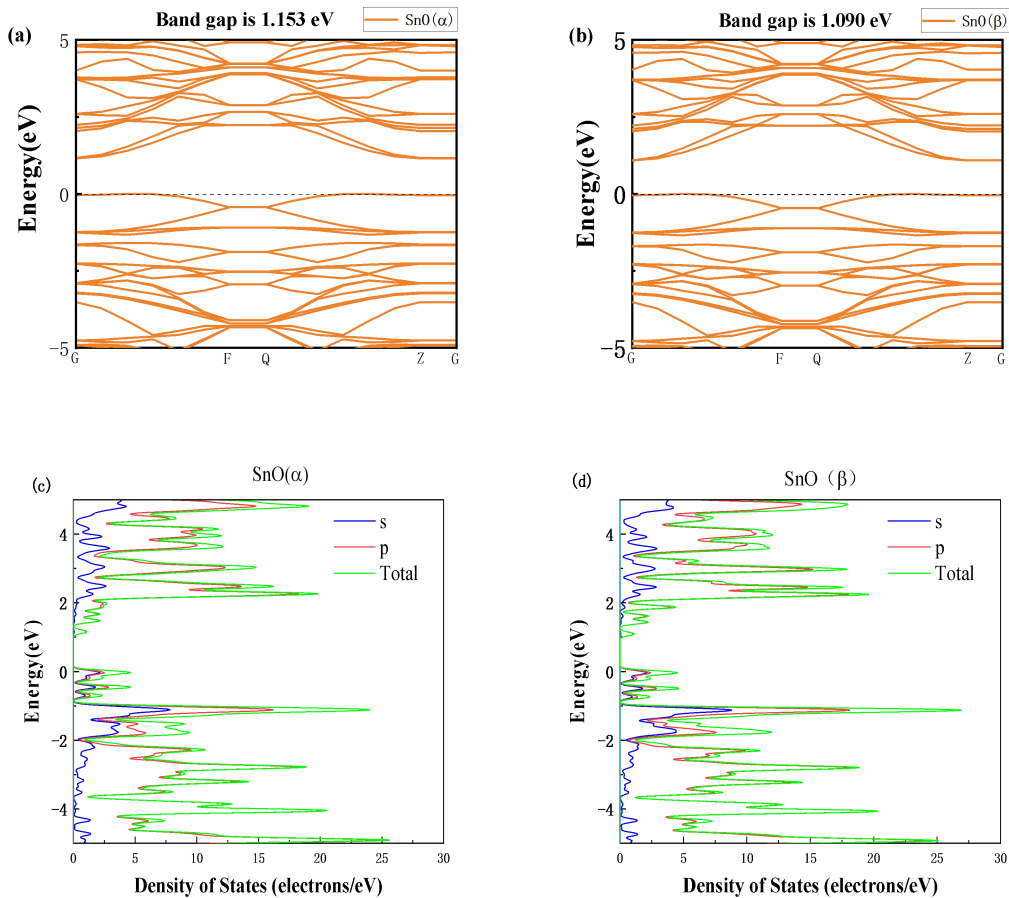


**Fig.3** Band Structure and density of states of SnO ( $\alpha$ ) and SnO ( $\beta$ )

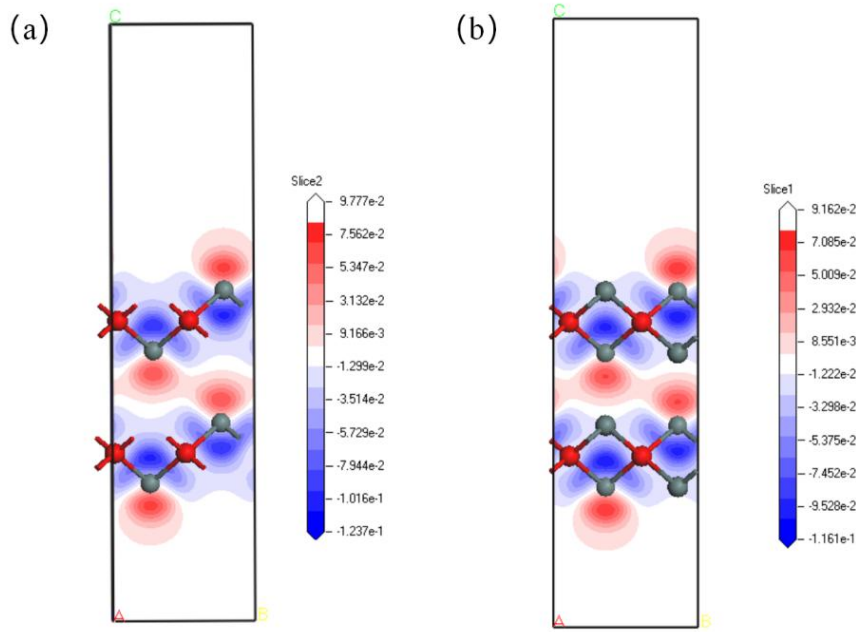


**Fig. 4** Deformation charge density of (a) SnO ( $\alpha$ ) and (b) SnO ( $\beta$ )

To explore more deeply the formation and distribution characteristics of the electronic energy band in SnO, this study calculated the total density of states and the partial density of states of SnO respectively. **Fig. 3** shows the calculated total density of states and partial DOS of SnO. In the total DOS, the Fermi level is within the range where the DOS value is zero, and the pseudogap is located in the vicinity of the Fermi level. In the partial density of states diagram, it can be clearly seen that the PDOS of the  $p$ -orbital exhibits significant pseudogap characteristics, and the unique electronic structure corresponding to SnO is coupled with its p-type conduction characteristics.

The deformation charge density is one of the important methods for studying the electronic structure. It is obtained by subtracting the atomic charge density at the corresponding points from the charge density after bonding. Through the calculation and analysis of the deformation charge density, we can clearly understand the migration of charges and the properties such as the bonding polarization direction during the bonding and bonding electron coupling processes. In **Fig. 4**, we use blue to represent the absence of electrons, red to represent the enrichment of electrons, and white to represent the regions where the electron density hardly changes. It can be found in **Fig. 4** that the Sn atoms are surrounded by blue, which means that Sn loses

electrons during the bonding process; the O atoms are surrounded by red, indicating that O gains electrons during the bonding process. Among them, the reddest regions of SnO( $\alpha$ ) and SnO( $\beta$ ) gain  $7.562 \times 10^{-1}$  electrons and  $7.085 \times 10^{-1}$  electrons respectively, and the bluest regions lose  $-1.237 \times 10^{-1}$  electrons and  $-1.161 \times 10^{-1}$  electrons respectively (the minus sign indicates the loss of electrons).

This is mainly due to the relatively low formation energy of tin vacancies (Sn), as well as the more dispersed hole transport channel - the valence band maximum (VBM) hybrid energy level formed by the hybridization of O 2p and spherical Sn 5s orbitals. During the formation of VBM, the Sn 5s orbital plays a dominant role. Since the Sn 5s orbital is spherical and the directionality of electron cloud overlap is not strong, this is more conducive to hole transport. Therefore, SnO has a relatively high hole mobility. According to **Fig. 3(a)**, the conduction band minimum energy level (CBM) of SnO mainly originates from the Sn 5p orbital, and its PDOS curve exhibits a free electron band, indicating that if there are a sufficient number of electrons, electrons can also move in SnO to generate an electric current. This series of research results provide important theoretical basis and experimental support for further understanding the electronic properties of SnO and its applications in related electronic devices.

The deformation charge density and electronic radius were used to calculate the deformation bond energies from **Eq. 15** as follows: -0.0675 and -0.0595 eV for SnO( $\alpha$ ) and SnO( $\beta$ ), respectively. The parameters of the deformation charge density and atomic radius of the deformation bond energy for SnO( $\alpha$ ) and SnO( $\beta$ ) obtained from the calculations are shown in **Table 3**.

**Table 3** Deformation charge density  $\delta\rho(\vec{r}_{ij})$  and deformation bond energy  $\delta V_{bc}(\vec{r}_{ij})$ , as obtained from the BBC model.

$$\left( \varepsilon_0 = 8.85 \times 10^{-12} C^2 N^{-1} m^{-2}, e = 1.60 \times 10^{-19} C, |\vec{r}_{ij}| \approx d_{ij} / 2 \right)$$

	SnO( $\alpha$ )	SnO( $\beta$ )
$r_{ij} (\text{Å})$	1.130	1.128
	Sn-O	Sn-O

$r_i ( \text{ \AA } )$	1.58 (Sn)	1.58 (Sn)
$\vec{r}_j ( \text{ \AA } )$	0.66 (O)	0.66 (O)
$\delta\rho^{\text{Hole-electron}} \left( \vec{r}_{ij} \right) \left( \frac{e}{\text{ \AA }^3} \right)$	-0.1237	-0.1161
$\delta\rho^{\text{Bonding-electron}} \left( \vec{r}_{ij} \right) \left( \frac{e}{\text{ \AA }^3} \right)$	0.0756	0.07085
$\delta V_{bc}^{\text{bonding}} \left( \vec{r}_{ij} \right) (\text{eV})$	-0.0675	-0.0595

### 3.3 Analytical approach of the renormalization group on energy scales

An energy scale  $L$  can be represented bond energy in the following way:

$$L = \frac{|V_i(\vec{r})|}{|V_0(\vec{r})|} = e^{-\mu r} \quad (20)$$

Where  $V_0(\vec{r}) = |\delta V_{bc}^{\text{bonding}}(\vec{r}_{ij})|$  and  $\mu$  is the charge-shielding factor[20]. The ultimate goal of studying energy scales is to resolve the corresponding physical information. The energy scale is a measure of bond energy, which determines the relaxation and strength of energy. It can be presented in the form of mathematical functions, whether linear or non-linear, and can adapt to the diversity of physical phenomena.

The potential energy surface function of bonds can be represented by wave functions:

$$\begin{cases} V_i(\vec{r}) = L \cdot V_0(\vec{r}) \cos k_x = V_0(\vec{r}) e^{-\mu r} \cos k_x & (1D) \\ V_i(\vec{r}) = L \cdot V_0(\vec{r}) (\cos k_x + \cos k_y) = V_0(\vec{r}) e^{-\mu r} (\cos k_x + \cos k_y) & (2D) \\ V_i(\vec{r}) = L \cdot V_0(\vec{r}) (\cos k_x + \cos k_y + \cos k_z) = V_0(\vec{r}) e^{-\mu r} (\cos k_x + \cos k_y + \cos k_z) & (3D) \end{cases} \quad (21)$$

**Eq. 21** can be used to plot the wave function diagram of the energy scale, as is shown in **Fig. 5**. The wave function of energy itself contains extremely rich physical information and shows obvious characteristics on different scales. For the image of

the energy wave function, on a large scale, it can display macroscopic features such as the overall energy trend, for example, the overall energy distribution of a quantum system. On a small scale, it provides subtle fluctuations and local changes, such as the slight differences in the particle probability distribution within a local area. The renormalization model accurately captures this multi-scale characteristic and finds a balance between different scales through reasonable processing, thereby realizing the effective transformation of the energy function.

To study the energy wave functions of  $\text{SnO}(\alpha)$ , we selected two different energy scale values,  $L=1.5$  and  $L=8$ , and substituted these values into **Eq. 21**, using the corresponding values from **Table 3**. The resulting formulas are as follows:

$$\begin{cases} V_i(\vec{r}) = 1.5 \cdot 0.0675 \cdot (\cos k_x + \cos k_y) & (2D) \\ V_i(\vec{r}) = 1.5 \cdot 0.0675 \cdot (\cos k_x + \cos k_y + \cos k_z) & (3D) \end{cases} \quad \begin{cases} V_i(\vec{r}) = 8 \cdot 0.0675 \cdot (\cos k_x + \cos k_y) & (2D) \\ V_i(\vec{r}) = 8 \cdot 0.0675 \cdot (\cos k_x + \cos k_y + \cos k_z) & (3D) \end{cases} \quad (22)$$

For  $\text{SnO}(\beta)$  ( $V_0(\vec{r}) = 0.0595$ ), the study can also be conducted by analogy with **Eq. 22**. Through these calculations, we obtained the wave function diagrams in **Fig. 5**, which illustrate the dynamic changes of the potential energy functions at different energy scales.

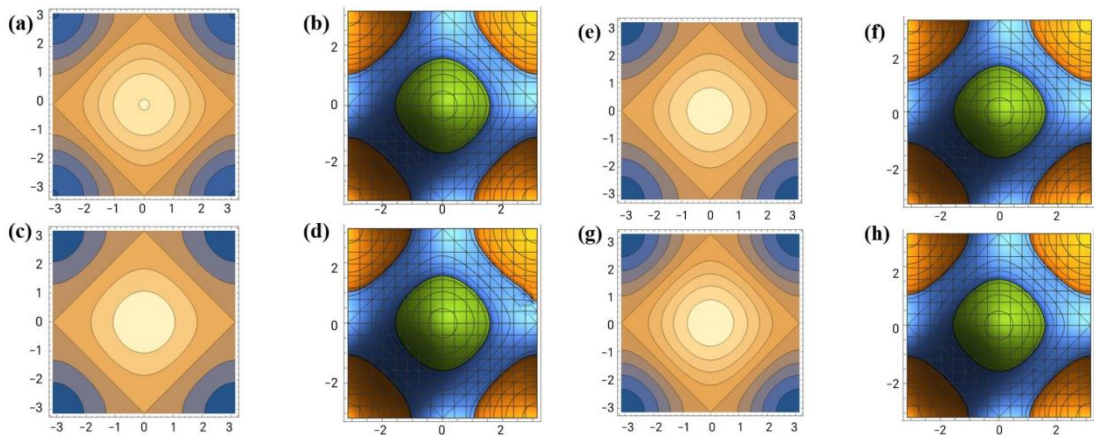


**Fig.5** shows the renormalized energy scale wave function diagrams for  $\text{SnO}(\alpha)$  and  $\text{SnO}(\beta)$ : (a) and (b) depict the renormalization of  $\text{SnO}(\alpha)$  in 2D and 3D spaces, respectively, when  $L=1.5$ ; (c) and (d) depict the renormalization of  $\text{SnO}(\alpha)$  in 2D and

3D spaces, respectively, when  $L=8$ ; and (e) to (h) depicting the renormalization of  $\text{SnO}(\beta)$  under the same conditions.

In the 2D case (**Fig.5a, c, e and g**),  $\text{SnO}(\alpha)$  exhibits different characteristics in its wave behavior. As  $L$  increases, the wave nature of  $\text{SnO}(\alpha)$  diminishes, which may indicate that its wave function tends to stabilize at larger energy scales(**Fig. 5a and c**). In contrast, for  $\text{SnO}(\beta)$  at the same  $L$  values, the distribution of the wave function becomes more refined, showing more wave-like characteristics (Fig. 5e and g). This could imply that there is some periodic wave feature at the energy scale. In the 3D case (**Fig.5 b, d, f and h**), the renormalized wave behavior exhibits more complex characteristics due to the increase in degrees of freedom.

Starting from **Eq. 10**, given that  $b < 1$ , when  $2n(d-2)-d > 0$ , the coupling constant  $\lambda_n$  decreases as the scale decreases, indicating that certain interactions become less significant at smaller scales and can thus be considered "irrelevant." Conversely, when  $2n(d-2)-d < 0$ , the coupling constant  $\lambda_n$  increases as the scale decreases, and these interactions are referred to as "relevant." When  $2n(d-2)-d=0$ , the coupling constant  $\lambda_n$  does not change with scale, a situation defined as "marginal." In scalar field theory, the most relevant interactions become marginal at the dimension known as the critical dimension in condensed matter physics. Taking the logarithm of both sides of **Eq. 10**, we can obtain

$$\ln(\lambda_n') = \left[ \frac{n}{2}(d-2) - d \right] \ln(b) + \ln(\lambda_n) \quad (23)$$

Differentiating the above equation with respect to the scale  $L$ , and based on  $b = 1 - (\delta\Lambda / \Lambda)$ , with the scale  $L = \Lambda^{-1}$ , we obtain  $\delta\Lambda = -\Lambda^2 dL$ , hence

$$L \frac{d\lambda_n}{dL} = - \left[ \frac{n}{2}(d-2) - d \right] \lambda_n \quad (24)$$

We have chosen the number of interacting fields  $n = 2$ , and the spatial



dimensions  $d = 2$  and  $d = 3$  as the subjects of our study, and substitute their values into Eq. 24 to explore the variation trend of the coupling constant  $\lambda_n$  with the energy scale  $L$ .

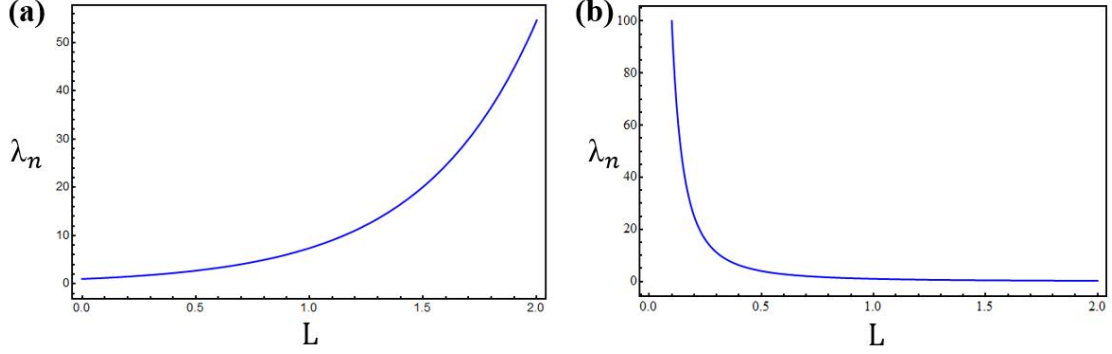


**Fig. 6** depicts the coupling constant versus energy scale.(a) illustrates the scenario for 3D space ( $d=3$ ), while (b) represents the 2D case ( $d=2$ ).

**Fig. 6** demonstrates the relationship between the energy scale  $L$  and the coupling constant  $\lambda_n$  in spaces of different dimensions. In 3D space (Fig. 6a), the coupling constant  $\lambda_n$  increases exponentially with the increase of  $L$ , indicating that in a 3D system, the coupling strength between two interacting fields grows rapidly with the increase in energy scale. Conversely, in 2D space (Fig. 6b), the coupling constant  $\lambda_n$  decreases as  $L$  increases, possibly due to the more limited interactions between particles in a 2D system, leading to a weakening of the coupling strength.

The renormalization group method is mainly used to deal with the behavior of physical systems at different scales. In physical systems, there are various interactions, and these interactions are described by coupling constants. When we consider the changes of the system at different scales, for example, the transition from the microscale to the macroscale, some details of the system may become unimportant, while some overall and key physical properties need to be retained.

In the field of theoretical physics research, especially in the discussion of critical phenomena and phase transitions, the renormalization group method plays a crucial role. This method enables us to analyze the behavior of a system at different scales, especially when the system is close to the critical point (quantum resolution limit).

Under this framework, coupling constants are used to describe the strength of interactions in the system, and their behavior as the scale changes can be described by differential equations. The key point is that even if the scale  $L$  is compressed, the main physical characteristics of the function can still be retained. This means that when we need to further analyze the scale  $L$ , such as calculating its energy eigenvalues and studying its correlation with other physical quantities, we can still perform accurate analysis based on the compressed function. Because during the compression process, we filter and retain the information that plays a key role in the overall physical properties through renormalization operations.

#### **4. Conclusion**

In this paper, the electronic and bonding properties of 2D stannous oxide materials were calculated using DFT. Through the calculation and analysis of the BBC model, the topological geometry of atomic bonds and the state of bonding electrons can be clearly obtained. In addition, the energy wave function was renormalized to determine the energy wave function under different quantum resolution sizes. The research shows that the coupling constant  $\lambda_n$  will change with the scale  $L$ . This study has greatly improved our understanding of the local bonding state and quantum resolution size on the surface of 2D structural materials.

#### **Acknowledgement**

Financial supports by the science and technology research Program of Chongqing Municipal Education Commission (Grant No. KJQN202401420)

## References

- [1] D.R. Kripalani, P.-P. Sun, P. Lin, M. Xue, K. Zhou, Vacancies and dopants in two-dimensional tin monoxide: An ab initio study, *Applied Surface Science* 538 (2021) 147988.
- [2] Y. Wang, S. Li, J. Yi, Transition metal-doped tin monoxide monolayer: a first-principles study, *The Journal of Physical Chemistry C* 122 (2018) 4651-4661.
- [3] K. Jiang, J. Ji, W. Gong, L. Ding, J. Li, P. Li, B. Li, F. Geng, Mechanical cleavage of non-van der Waals structures towards two-dimensional crystals, *Nature Synthesis* 2 (2023) 58-66.
- [4] J.P. Allen, D.O. Scanlon, S.C. Parker, G.W. Watson, Tin monoxide: Structural prediction from first principles calculations with van der waals corrections, *The Journal of Physical Chemistry C* 115 (2011) 19916-19924.
- [5] W. Zhou, N. Umezawa, Band gap engineering of bulk and nanosheet SnO: an insight into the interlayer Sn–Sn lone pair interactions, *Physical Chemistry Chemical Physics* 17 (2015) 17816-17820.
- [6] D. Aurbach, A. Nimberger, B. Markovsky, E. Levi, E. Sominski, A. Gedanken, Nanoparticles of SnO produced by sonochemistry as anode materials for rechargeable lithium batteries, *Chemistry of materials* 14 (2002) 4155-4163.
- [7] K.J. Saji, Y.V. Subbaiah, K. Tian, A. Tiwari, P-type SnO thin films and SnO/ZnO heterostructures for all-oxide electronic and optoelectronic device applications, *Thin Solid Films* 605 (2016) 193-201.
- [8] A. Mubeen, A. Majid, M. Alkhedher, S. Haider, M.S. Akhtar, First principles investigations on electronic and magnetic properties of Fe: SnO monolayer, *Optical and Quantum Electronics* 55 (2023) 914.
- [9] A. Mubeen, A. Majid, First principles investigation of 3d transition metal doped SnO monolayer based diluted magnetic semiconductors, *Journal of Magnetism and Magnetic Materials* 580 (2023) 170897.
- [10] Y. Ge, Y. Liu, Effects of layer stacking and strain on electronic transport in two-dimensional tin monoxide, *Chinese Physics B* 28 (2019) 077104.
- [11] Y. Ogo, H. Hiramatsu, K. Nomura, H. Yanagi, T. Kamiya, M. Hirano, H. Hosono, p-channel thin-film transistor using p-type oxide semiconductor, SnO, *Applied Physics Letters* 93 (2008).
- [12] Y.F. Cheng, Z. Li, M. Zhang, H.G. Xie, T. Tang, Y. Liang, X.X. Wang, K. Xu, B.Y. Zhang, A.A. Haidry, Liquid-tin-printed two-dimensional SnO for optoelectronic NO<sub>2</sub> gas sensing at room temperature, *Journal of Materials Chemistry C* 11 (2023) 14187-14198.
- [13] A. Hunanyan, N. Petrosyan, H. Zakaryan, Gas sensing properties of two dimensional tin oxides: A DFT study, *Applied Surface Science* 672 (2024) 160814.
- [14] L. Wanzhong, S. Jian, D. Chong, Layer-dependent electronic and optical properties of tin monoxide: A potential candidate in photovoltaic applications, *Physical Chemistry Chemical Physics* 24 (2022) 7611-7616.
- [15] J.P. Allen, D.O. Scanlon, L.F. Piper, G.W. Watson, Understanding the defect chemistry of tin monoxide, *Journal of Materials Chemistry C* 1 (2013) 8194-8208.
- [16] J. Heyd, G.E. Scuseria, M. Ernzerhof, Hybrid functionals based on a screened Coulomb potential, *The Journal of chemical physics* 118 (2003) 8207-8215.
- [17] T. Sasamoto, H. Spohn, One-dimensional Kardar-Parisi-Zhang equation: an exact solution and its universality, *Physical review letters* 104 (2010) 230602.
- [18] A. Zee, *Quantum field theory in a nutshell*, Princeton university press 2010.

[19] Y. Tan, M. Bo, Non-Hermitian Bonding and Electronic Reconfiguration of Ba<sub>2</sub>ScNbO<sub>6</sub> and Ba<sub>2</sub>LuNbO<sub>6</sub>, *Annalen der Physik* 536 (2024) 2400040.

[20] L. Ge, M. Bo, Atomic bonding states of metal and semiconductor elements, *Physica Scripta* 98 (2023) 105908.